Unveiling the interaction of reactions and phase transition during thermal abuse of Li-ion batteries

F. Baakes [a], M. Lüthe [b], M. Gerasimov [a], V. Laue [c], F. Röder [d], P.B. Balbuena [e], U. Krewer [a,*]

[a] *Institute for Applied Materials – Electrochemical Technologies, Karlsruhe Institute of Technology, Adenauerring 20b, Karlsruhe 76131, Germany*
[b] *Institut für Thermodynamik, Technische Universität Braunschweig, Hans-Sommer-Str. 5, 38106 Braunschweig, Germany*
[c] *Institute of Energy and Process Systems Engineering, Technische Universität Braunschweig, Langer Kamp 19B, Braunschweig 38106, Germany*
[d] *Bavarian Center for Battery Technology (BayBatt), University of Bayreuth, Universitätsstraße 30, 95447 Bayreuth, Germany*
[e] *Department of Chemical Engineering, Texas A & M University, College Station, Texas 77843, United States*

HIGHLIGHTS

- First time consideration of phase equilibria in Li-ion battery thermal runaway.
- Complex interaction of SEI degradation, reformation and solvent boiling revealed.
- Fragile equilibrium of endo- and exothermic processes in self-heating phase.
- Unpredictability of thermal runaway related to presence of LEDC or water.
- Rising pressure from reaction gases can suppress solvent boiling.

GRAPHICAL ABSTRACT
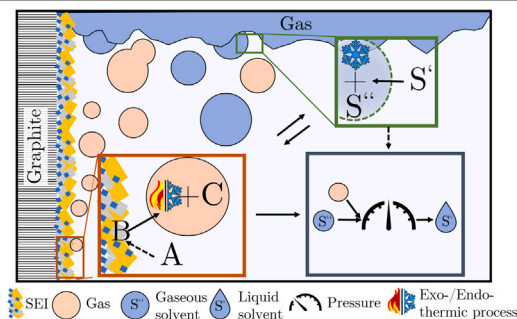
ARTICLE INFO

ABSTRACT

Safety considerations have always accompanied the development of new battery chemistries; this holds especially for the Li-ion battery with its highly reactive components. An overall assessment and decrease of risks of catastrophic failures such as during thermal runaway, requires an in-depth and quantitative understanding of the ongoing processes and their interaction. This can be provided by predictive mathematical models. Thus, we developed a thermal runaway model that focuses on rigorous modelling of thermodynamic properties and reactions of each component within a Li-ion battery. Moreover, the presented model considers vapour–liquid equilibria of a binary solvent mixture for the first time. Simulations show a fragile equilibrium between endothermic and exothermic reactions, such as $LiPF_6$ and LEDC decomposition, in the early phases of self-heating. Further, an autocatalytic cycle involving the production of HF and the SEI component Li_2CO_3 could be revealed. Additionally, the unpredictability of the thermal runaway could be directly correlated to availability of LEDC or contaminants such as water. Also, solvent boiling can have a significant influence on the self-heating phase of a Li-ion battery, due to its endothermic nature. Further analysis revealed that the rising pressure, stemming from gassing reactions, can suppress solvent boiling until the thermal runaway occurs.

1. Introduction

During their development in the 80's it was revealed that Li-ion batteries are safer alternatives to lithium metal based secondary batteries [1–3]. Still, potential safety hazards under high temperature abuse exist and have already been known during and before commercialization [2,4–7]. Since then, Li-ion batteries have made their way into nearly all parts of our daily life. However, progression into electric mobility and the constantly increasing energy densities made consideration of safety an omnipresent accompanying issue [8–12]. The most dangerous safety hazard is the thermal runaway, which is caused by a cascade of exothermic reactions and which led to high-profile images of burning electric cars in the media [13–15]. Despite extensive experimental analysis, there are still a lot of unanswered question. It remains largely uncertain, when and if a battery will go into thermal runaway, and what could prevent it.

Various experiments are used to obtain a deeper insight into batteries and their safety. The most common ones are Differential Scanning Calorimetry (DSC) and Accelerated Rate Calorimetry (ARC) [11,16–19]. In both methods the battery cell is heated and the response in terms of released energy is observed. Yet, the way of observation differs. In a DSC measurement, a fixed heating-rate is applied to the probe and a reference. From the difference in their temperature change the exothermic or endothermic heat flow is concluded. Further, temperature ranges in which specific reactions start have been recorded by means of DSC in prior works [20,21]. In contrast, in an ARC measurement, a sample is preheated to a given temperature, then an equilibration period is performed. This is followed by a seek period in which it is repeatedly checked if a certain threshold of self-heating is exceeded. This mode is called Heat-Wait-Seek (HWS) mode. In the case of self-heating, the method switches to adiabatic operation, i.e. without external heating and cooling. In this so called exotherm mode the setup tracks and follows the temperature evolution of the sample until reaching a set temperature, e.g. several 100 degrees for thermal runaway studies. Aside the mentioned experiments many other safety analysis methods such as nail penetration, crush-tests and oven tests are used to characterize battery safety [22–24].

Experiments do not allow a direct conclusion on the occurring processes inside of the battery. Here, the coupling of experiments and mathematical battery models is a highly potent approach that allows insight into the underlying processes and to develop effective counter measures [24–29]. Due to the complexity and variety of phenomena during the thermal runaway, building a comprehensive model that covers all occurring effects is an ongoing effort [30].

As the processes connected to battery safety are multiple, models developed to investigate them are as well. Some models focus on the temperature distribution and heat propagation within cells or battery stacks [31,32]. Others investigate the effect of short-circuits as a cause of thermal events within batteries [33–35]. However, as our focus is on the interaction of chemical reactions and other processes related to chemical compounds of the cell, the following literature survey will focus on these types of models.

First models, using a one-step substitute reaction by Richard et al. [25], suggested the initial decay of the solid electrolyte interphase (SEI) as the primary cause of initial self-heating in an ARC measurement. The model was later extended such that three substitute reactions, representing the SEI degradation, reaction of intercalated lithium with the electrolyte and the positive active material degradation, could replicate an oven test for a whole Li-ion cell [24]. Based on these prior studies Kim et al. developed a three dimensional battery model including four degradation reactions, now also considering electrolyte decomposition [28]. These kind of reaction models have then been used in several other model types, which are focusing on different aspects of battery safety such as the ones mentioned above. However, these models are not considering the battery's chemical compounds. This simplification enabled them to calculate highly discretized temperature distributions of cells or whole battery packs [11,

28,29,31]. The downside is the inability to understand the interaction of the actual cell composites due to the missing balance of reactants and products as well as the individual influence of each component on the released heat.

Detailed chemical models exist especially on the atomistic scale. Here, in previous work we made use of molecular simulation to study the formation of the SEI. With this we identified a multitude of crucial reaction pathways [36,37]. Additionally, there are multi-scale models which on the one side still allow for a heterogeneous SEI description based on kinetic Monte Carlo and on the other side also allow for concentration and potential profiles in the cell. This is achieved by coupling kinetic Monte Carlo to continuum scale models with charge and mass balances, and it enables the simulation of SEI growth during the full formation process and during discharge [38,39]. However, such molecular and multiscale models span usually only short time scales, below microseconds for the molecular ones, and only few cycles for the latter one. They further require presently very long computation times. Here continuum models with detailed micro kinetics come into play, which can be parameterized with both, molecular simulation or (preferably dynamic) experiments [40,41]. To the best of our knowledge, the first approach to include actual battery chemistry in processes connected to high temperature battery degradation was done by Tanaka in 2013 who simulated the SEI decomposition reaction based on the chemistry of lithium ethylene dicarbonate (LEDC) as the major SEI composite [42]. Kupper et al. extended this approach by including SEI specific calendaric aging mechanisms at various temperatures into a Pseudo 3D electrochemical model. Besides complex electrochemical charge transfer and aging reactions, heat and mass transport processes are implemented in their framework. Thereby, they were able to capture the nonlinear relationship between calendaric aging, performance and temperature [43].

In these preceding studies, the aging behaviour in regards to the SEI growth and decomposition was focused. However, the thermal runaway, like most reaction related phenomena in batteries [36,41, 44,45], consists of a complex reaction network including degradation of all battery components [27]. Additionally, phase transitions of the liquid electrolyte components are induced due to the rapid temperature increase caused by the thermal runaway. This phenomenon has up until now only been studied in connection to the venting of cells [46,47]. However, boiling is an endothermic process and its interaction with exothermic degradation reactions as well as their influence on the self-heating behaviour during thermal abuse have not yet been studied. Thus we identified the following open questions:

- How do occurring reactions during the thermal runaway interact with each other and how would boiling of the electrolytes' solvent components influence this interaction.
- To what extent does the pressure build-up through evolution of gaseous degradation products influence the phase transition behaviour?

In order to address these questions, we developed and analysed a thermal runaway model which focuses on crucial chemical compounds, their reactions and thermodynamic properties such as aggregate phases. This, for the first time, allows for a detailed investigation of the occurring reactions, their interaction and influence on the self-heating phase during thermal abuse of Li-ion batteries. To incorporate the phase transition, binary solvent phase equilibria models were implemented. After introducing the parameter identification approach and model, the model is then used to reveal the complex course of events during an ARC measurement of a Li-ion battery. Special focus is laid on analysing the primary stages during the self-heating phase, between 90 °C and 130 °C, where a fragile equilibrium between exothermic events such as degradation reactions and endothermic processes such as boiling is present. Ultimately, the influence of evolving reaction gases on the phase transition behaviour is illuminated. In future this approach will allow to develop counter measures and extend analysis to the influence of species, such as SEI components or impurities like water, on the safety behaviour of batteries including new cell chemistries.
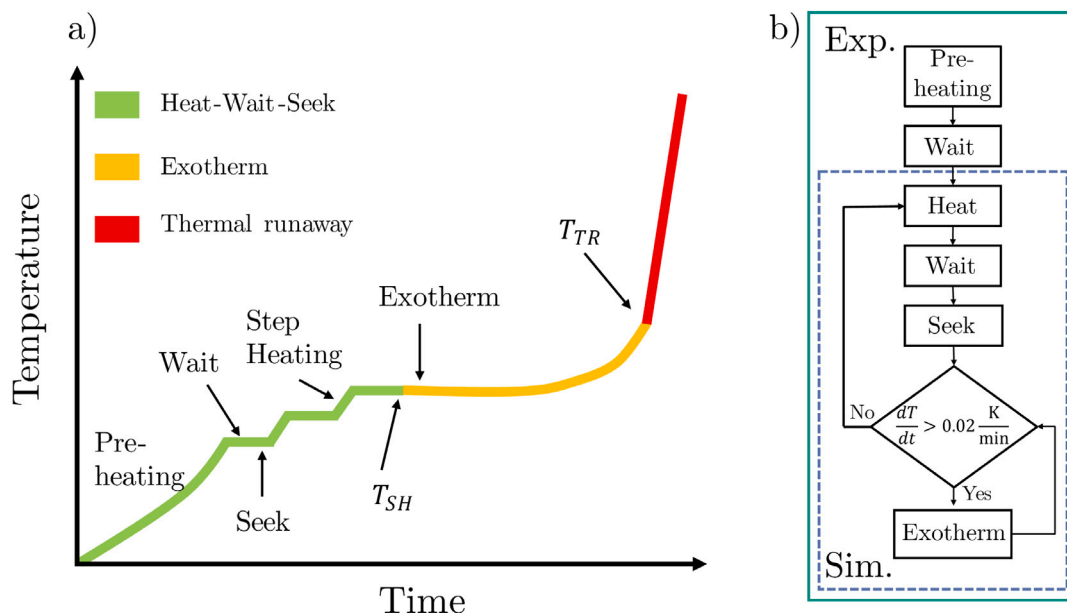
Fig. 1. (a) General illustration of an ARC measurement adapted from Townsend et al. [52] with the characteristic temperatures of self-heating and thermal runaway T_{SH} and T_{TR}, respectively. (b) Flowchart description of Accelerated Rate Calorimetry algorithm subdivided into the more general experimental green part and the implemented blue part. (For interpretation of the references to colour in this figure legend, the reader is referred to the web version of this article.)

2. Methods

In the following section we introduce the test case of a thermal runaway which is simulated, the experimental data, the assumed processes, the model and finally its parameterization.

2.1. Test case and experimental data

For this study, we choose to investigate self-heating and thermal runaway using ARC because this type of measurement allows to study and determine the crucial initial phase of the transition into self-heating of the battery as well as the further transition into thermal runaway.

The left hand side of Fig. 1 graphically explains the afore described general progression of an ARC measurement. Here the three different stages have been marked in green (Heat-Wait-Seek), yellow (Exotherm) and red (Thermal runaway). Note that the second phase, here called exotherm mode, has different names assigned to it in literature. The most common ones are: exotherm mode, adiabatic mode and self-heating phase [48–50]. In this publication exotherm mode is used when referring to the experimental set-up, and the term self-heating phase when describing the behaviour of the investigated battery. However, all terms describe the same stage and could also be used interchangeably. Additionally, two essential temperatures, the on-set temperature of self-heating T_{SH} is marked and the on-set temperature of thermal runaway T_{TR}, defined as the point, where the temperature gradient [51] exceeds $\frac{dT}{dt} = 10\,\mathrm{K\,s^{-1}}$. The right hand side shows a more detailed variant in a flowchart.

Experimental data from Maleki et al. [17] was chosen because the chemistry is close to the ones used today. In addition, since the experiments were carried out with a commercial cell in 1999, it is safe to assume that no SEI forming additives like vinylene carbonate (VC) have been added. This is due to the fact that the first patent covering the usage of VC as an additive for LIB's has only been filed in 1998, and first research articles investigating the effects of VC have not been published before 2002 [53,54]. Malekis experiments are thus also assumed to not contain any formation and degradation of polymeric SEI components resulting from VC degradation. The cell used for the experiments had a capacity of 550 mAh. The chemistry was reported to be a carbon based anode, a $LiCoO_2$ cathode, polyvinylidenefluoride (PVdF) as binder in both electrodes and a ethylene carbonate (EC)/ethyl methyl carbonate (EMC) mixture with $LiPF_6$ as the conductive salt. Yet, since the original publication is lacking additional data, some assumption have to be made to achieve a proper set of initial and boundary conditions for the simulation (see Section 2.3). The full set of calculations used to obtain the initial conditions can be found in the SI and all used structural as well as component specific physical parameters.

2.2. Assumed reactions and further processes

During and before the thermal runaway, a multitude of different reactions can take place. As the used ARC measurement only spans a temperature range up to 220 °C, only reactions and phenomena known to occur in this range are in the focus of this work. The main reactions that are assumed to occur and which are thus selected for this work are summarized in Table 1, with their respective literature reference, temperature span at which they start to be visible in DSC and ARC, and the abbreviation of the reaction used in this work.

The kinetic parameters of the reactions determine when and how fast each reaction takes place during the runaway at a given temperature and composition. They are thus essential for understanding and modelling the thermal runaway. The kinetic parameters are unknown and are hence identified from the ARC measurement described before. For the parameterization of the activation energies $E_{A,i}$ and the reaction rate constants $k_{0,i}$ of all considered reactions i, we take into account the following behaviour reported in literature. The initial breakdown of the SEI is widely assumed to be responsible for the first exothermic reactions leading to the transition from HWS mode in the ARC measurement to exotherm mode [25]. For this, the decomposition of the main SEI components, LEDC and Li_2CO_3 are considered. Salt decomposition to PF_5 and the subsequent decomposition of PF_5 to the highly reactive HF is also known to take place in a similar temperature range and is assumed to impact ARC measurement. Thus, both reactions are considered as well. The reported temperature span for the decomposition of the primary SEI is extremely wide, as it ranges from 60 °C to 120 °C[11, 17,67,68]. The SEI and salt decomposition reactions are followed by the re-formation of SEI and its main components, Li_2CO_3 and LEDC. The combination of SEI build-up and the subsequent re-decomposition is mainly held accountable for the long self-heating period, before

Table 1

Degradation reactions and the temperature ranges in which the reactions are observed in DSC and ARC measurements.

Category	Abbreviation	Eq.	T_{start}/°C
Organic SEI decomposition [55,56]	OSD	$(CH_2OCO_2Li)_2 \longrightarrow Li_2CO_3 + C_2H_4 + CO_2 + 0.5\,O_2$	60–120
Inorganic SEI decomposition [57,58]	ISD	$Li_2CO_3 + 2\,HF \longrightarrow 2\,LiF + H_2O + CO_2$	60–120
Organic SEI production [59]	OSP	$2\,LiC_6 + 2\,C_3H_4O_3 \longrightarrow (CH_2OCO_2Li)_2 + C_2H_4 + 2\,C_6$	120–200
Inorganic SEI production [60]	ISP	$2\,LiC_6 + C_3H_4O_3 \longrightarrow Li_2CO_3 + C_2H_4 + C_6$	120–200
Conductive salt decomposition [21,60–63]	CSD	$LiPF_6 \longrightarrow LiF + PF_5$	60–80
HF production [21,60,61,64]	HFP	$PF_5 + H_2O \longrightarrow 2\,HF + POF_3$	60–80
EC decomposition [27,65]	ECD	$2.5\,O_2 + C_3H_4O_3 \longrightarrow 3\,CO_2 + 2\,H_2O$	180–350
EMC decomposition [27,65]	EMCD	$4.5\,O_2 + C_4H_8O_3 \longrightarrow 4\,CO_2 + 4\,H_2O$	180–350
Cathode decomposition [17,20,66]	CD	$Li_zCoO_2 \longrightarrow zLiCoO_2 + \frac{1-z}{3}Co_3O_4 + \frac{1-z}{3}O_2$	150–220

the actual thermal runaway starts (see Fig. 1) [27,69]. The thermal runaway itself, which starts at a higher temperature around 150 °C is generally assumed to be strongly connected to the decomposition of the cathode and the subsequent combustion of solvent molecules by released oxygen [56,65].

Besides these reactions, the following reactions are reported but will not be considered in this work. The reaction $Li_2CO_3 \longrightarrow Li_2O + CO_2$ is not considered even though the experiments of Abraham et al. [67] reported an extensive amount of Li_2O in cells quenched at 150 °C compared to ones cycled at room temperature. However, the mentioned reaction is reported to only occur around 800 °C [70] without the addition of catalyzing species. Transitions metals like cobalt, nickel and manganese present in the positive active material of Li-ion batteries are already assumed to have such an effect [71]. This could explain the measured Li_2O, despite no different reaction path connected to thermal abuse of batteries has been proposed yet. A sound integration of Li_2O reactions would thus require more in-depth prior studies. The reaction of active material with the binder PVdF is attributed to reactions happening around 300 °C, which is outside the considered temperature range. The interaction between the conductive salt and the breakdown of the primary SEI, reactions CSD, HFP and IDS in our study, has been proposed differently by Eshetu et al. [72]. They suggested a direct reaction of PF_5 with Li_2CO_3 as well as LEDC without the intermediate formation of H_2O and HF. This only works under the assumption that the formation of these intermediates is not rate determining. Since this is for now not known we implemented these as the two-step reactions described above.

Also, reactions involving materials like conductive agents and the current collectors are not considered. Whereas they may play a role in long-term battery aging due to overcharging or high current operation, to the best of our knowledge, there are no reactions reported for high temperature abuse [73]. Additionally, the separator is not considered as well since for PP/PE separators, aside melting [69], no reactions are reported, for the context of thermal runaway. However, some reactions are reported in the context of electrolyte degradation with glass fibre separators [74]. Both aspects are not included in our current work, however, they might be of interest for future investigations.

Aside from these reactions, the boiling of electrolyte may occur during cell heating. The effect is usually ignored in other literature works, but as it is a potential heat sink that allows to stabilize the temperature, we deem it important to include this aspect into our analysis to get a full picture of process sensitivities and process interactions. The boiling temperature of the mixture depends on the assumed electrolyte composition and the pressure which here are assumed to be a 1/1 v/v EC/EMC mixture under isobaric atmospheric pressure. The boiling temperature is, for this initial composition, given with $T_{b,Mixture} = 122.45$ °C. This we calculated by a binary mixture phase equilibrium model of EC/EMC which we present in the SI.

2.3. Mathematical model

In this section the modelling approach is layed out. First, the modelled system and the underlying assumptions are presented. This is followed by a more detailed description of kinetics and the respective species and energy balances, including calculations of the exo- and endothermic heats. Eventually, the solubility model is outlined.
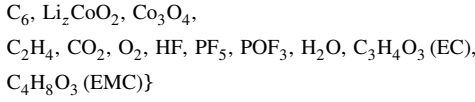
2.3.1. Model overview

The modelled scenario is the ARC measurement of Maleki et al. [17], conducted at OCV and an SOC of 100%. Adiabatic conditions in the seek and during self-heating periods are assumed. The system is closed. Self-heating and thermal runaway are driven by the heat of reaction released or consumed. Thus a crucial component of the presented model approach is the calculation of reaction heats from the enthalpies of formation of participating components by Hess's law [75]. This approach has already been utilized for degradation models, first by Tanaka et al. and later by Kupper et al. [42,43]. All modelled species and their physical parameters can be found in the SI. Furthermore, an approach for the calculation of the heat of boiling of a binary electrolyte mixture based on an equilibrium model is proposed. Finally, the individual contribution of each reaction or phase change to the overall produced heat can be calculated and a correlation between the balance of the species and the heat sinks and sources can be drawn. To allow a first investigation of the principle interaction of reaction and phase change during thermal abuse of a lithium-ion battery, diffusion and thermal conductivity are not implemented. The distinction between the different phases inside of a battery is done by four reference phases: the anode including the SEI, the liquid electrolyte, the cathode and a gas phase. The following further assumptions are underlying this modelling approach:

- Ideal mixed solution — no spatial discretization. Since the time constant for diffusion and thermal conductivity is in seconds and the ARC measurement takes hours, we deem the assumption of a perfectly mixed system a sound approach for this first study.
- No pressure increase due to gas evolution. This assumption corresponds to the initial stages of a highly inflatable pouch cell.
- Within each time step the solvent is in vapour–liquid equilibrium.
- Salt and its degradation products do not impact the vapour–liquid equilibrium.
- Reactions are irreversible and pseudo-homogeneous.
- The electrolyte consists of a 1/1 v/v mixture of EC and EMC with $1200\,\mathrm{mol\,m^{-3}}$ $LiPF_6$.
- The geometry of the cell is assumed to be similar to a commercially available one of the same capacity as the one used in this study [76].
- The electrode geometry is similar to other published electrodes of the same chemistry [77,78].
- The threshold for the battery self-heating rate is set to $0.02\,\mathrm{K\,min^{-1}}$ as reported in other publications including ARC tests which were conducted by Maleki et al. [79].
- The preheating is neglected in the simulation since it does not supply further information.

2.3.2. Set definitions

In the following sections, set notation is used for the sake of brevity and completeness. The first set Ω_{SP} contains all modelled chemical species. Abbreviations that are subsequently used to refer to certain species are added in brackets.

$\Omega_{SP} = \{(CH_2OCO_2Li)_2$ (LEDC), Li_2CO_3, LiF, $LiPF_6$, LiC_6,

C_6, Li_zCoO_2, Co_3O_4,

C_2H_4, CO_2, O_2, HF, PF_5, POF_3, H_2O, $C_3H_4O_3$ (EC),

$C_4H_8O_3$ (EMC)}

As the species occur in different phases or reactions, subsets of Ω_{SP} are defined as follows:

$\Omega_G = \{g \in \Omega_{SP} \mid \text{species } g \text{ is in gas phase}\}$

$\Omega_L = \{l \in \Omega_{SP} \mid \text{species } l \text{ is in liquid phase}\}$

$\Omega_S = \{s \in \Omega_{SP} \mid \text{species } s \text{ is in solid phase}\}$

$\Omega_K = \{k \in \Omega_{SP} \mid \text{species } k \text{ is reactant of reaction } j\}$

The subsets Ω_{Solv} and Ω_{SEI} describe the components of the solvent and the SEI, respectively.

$\Omega_{Solv} = \{C_3H_4O_3, C_4H_8O_3\} \subseteq \Omega_{SP}$,

$\Omega_{SEI} = \{(CH_2OCO_2Li)_2, Li_2CO_3, LiF\} \subseteq \Omega_{SP}$

Moreover the set Ω_{RE} lists all modelled reactions, with abbreviations added in brackets. The reaction equations are summarized in Table 1.

$\Omega_{RE} = \{$Organic SEI decomposition (OSD),

      Inorganic SEI decomposition (ISD),

      Cathode decomposition (CD)

      Organic SEI production (OSP), Inorganic SEI production (ISP),

      Conductive salt decomposition (CSD),

      HF production (HFP), EC decomposition (ECD),

      EMC decomposition (EMCD) }

2.3.3. Species balances and reaction kinetics

Since the battery is modelled as a closed system, there is no molar flux in or out of the battery. This yields the following species balance for all species i and respective reactions j:

$$\frac{dn_i}{dt} = \sum_{j \in \Omega_{RE}} \nu_{ji} r_j, \forall i \in \Omega_{SP}. \tag{2}$$

Here, n_i is the amount of species i, ν_{ji} refers to the stoichiometric coefficient of component i in reaction j and r_j refers to reaction rate of reaction j. If not mentioned otherwise, the reaction kinetics are modelled as power law kinetics combined with Arrhenius law to describe the temperature dependency [80,81]:

$$r_j = k_{0j} \exp\left(\frac{-E_{Aj}}{RT}\right) \prod_{k \in \Omega_K}, \forall j \in \Omega_{RE} \backslash \{OSP, ISP, CSD\}. \tag{3}$$

Here, k_{0j} refers to the pre-exponential factor for reaction j and E_{Aj} the respective activation energy. The dimensionless activity of each participating component is written as a_k and their definition is given in Section 2.3.5.

Eq. (4) represents a special case for reactions of intercalated lithium with the solvent that also take the thickness of the SEI-layer d_{SEI} into account since SEI growth is known to depend on SEI thickness [43]:

$$r_j = k_{0,j} \frac{1}{d_{SEI}} \exp\left(\frac{-E_{A,j}}{RT}\right) \prod_{k \in \Omega_K} a_k^{\nu_{k,j}}, \forall j \in \{OSP, ISP\} \tag{4}$$

Furthermore, it is widely assumed that for the decomposition of the conductive salt $LiPF_6$, only the non-dissociated part, as in the left hand site of $LiPF_6 \rightleftharpoons Li^+ + PF_6^-$, is decomposed [61]. Therefore the dissociation constant α is introduced in the salt decomposition rate to describe this phenomenon [18]. The constant is set to $\alpha = 0.7$ as already described by Stich et al. [61].

$$r_j = k_{0,j}(1 - \alpha) \exp\left(\frac{-E_{A,j}}{RT}\right) \prod_{k \in \Omega_K} a_k^{\nu_{k,j}}, \forall j \in \{CSD\} \tag{5}$$

As the ARC is conducted under OCV, no electrochemical reactions are implemented.

2.3.4. Energy balance, heat of reaction and phase change

The model for the temperature evolution is divided into two parts as illustrated in Fig. 1(b). In the first part the step-heating is modelled using a simple controller with one constant as follows:

$$\frac{dT}{dt} = \frac{T_{Setpoint} - T}{K}. \tag{6}$$

Here, $T_{Setpoint}$ corresponds to the temperature set by the ARC-algorithm which increases by $10\,°C$ after each HWS-step. K is a time constant that is chosen such that the step-heating could be reproduced accurately. In this simplified approach, the Heat period, where the temperature step is performed, and the Wait period, where the cell is given time to equilibrate with the temperature of the device in the experiment are joined together. This is done, since in our simulation only the cell temperature is simulated and the cell is not discretized. Thus, the cell is always in equilibrium. After the Heat-Wait period, the temperature evolution is calculated as follows within the Seek period:

$$\frac{dT}{dt} = \frac{\sum_{j \in \Omega_{RE}} q_j + q_{PT}}{C_{p,bat}}, \tag{7}$$

where q_j and q_{PT} refer to the rate of production of heat from reaction j and of the heat from phase transition of the electrolyte, respectively. If at the end of the Seek period the self-heating rate of the battery exceeds $\frac{dT}{dt} = 0.02\,\text{K min}^{-1}$, the temperature evolution is further calculated as in Eq. (7) corresponding to the exothermic mode of the ARC. Otherwise another Heat and Wait period as in Eq. (6) is performed. For the calculation of Seek periods as well as during exotherm mode, quasi-adiabatic conditions are assumed for the energy balance due to the experimental set-up explained in Section 2.1. Thus, the balance equation reduces to the form above, containing only heat sinks or sources due to reaction or phase change.

The isobaric heat capacity of the battery $C_{p,bat}$ is calculated from the individual components as follows:

$$C_{p,bat} = \sum_{i \in \Omega_{SP}} \underline{c}_{p,i} n_i + C_{p,Al} + C_{p,Cu} + C_{p,Casing}. \tag{8}$$

The parameters $c_{p,i}$, $C_{p,Al}$, $C_{p,Cu}$ and $C_{p,Casing}$ represent the molar heat capacity of component i, the heat capacity of the aluminium and copper current collector and the casing (in this case pouch-cell foil), respectively (see SI for more information).

The rate of heat produced or consumed in each reaction j is the product of their respective reaction rate r_j and the molar heat of reaction $\Delta_r \underline{H}_j$:

$$q_j = -r_j \Delta_r \underline{H}_j(T), \forall j \in \Omega_{RE}. \tag{9}$$

The heat consumption rate resulting from the transition of the liquid solvents of the electrolyte from liquid state $'$ to their gaseous state $''$ is calculated as:

$$q_{PT} = \sum_{\sigma \in \Omega_{Solv}} \frac{dn''_\sigma(T, p, x_{EC})}{dt} \cdot \Delta_{vap} \underline{H}_\sigma(T), \tag{10}$$

where $\Delta_{vap} \underline{H}_\sigma$ represents the vaporization enthalpy of solvent σ and $\frac{dn''_\sigma(T, p, x_{EC})}{dt}$ is the boiling rate of solvent σ which is calculated based on equilibrium data for T, p and compositions x_{EC}. The exact procedure is explained in the SI.

2.3.5. Solubility model — Concentration, partial pressure and activity

The calculations of concentrations and partial pressures are based on the four different phases where the reactions occur. Therefore the concentration in the liquid phase C_i is calculated as:

$$C_i = \frac{n'_i}{V}, \forall i \in \Omega_{SP}, \tag{11}$$

where V refers to the given reference volume listed in Table 2 (a detailed description how the volumes are calculated is given in the SI). n'_i refers to the liquid part if the species exists either in liquid or gas form.

The partial pressure p_g of gas g is given as the product of the mole fraction of the component in the gas phase x_g'' and the given system pressure as stated through Dalton's law [82]

$$p_g = p \cdot x_g'', \forall g \in \Omega_G. \tag{12}$$

The system pressure is set to $p = 101\,325\,\text{Pa}$ and as isobaric conditions are assumed, the value is kept constant during the whole simulation. Activities are then defined as follows:

$$a_l = \frac{C_l}{C^\ominus}, \forall l \in \Omega_L \text{ and} \tag{13}$$

$$a_s = \frac{C_s}{C^\ominus}, \forall s \in \Omega_S \text{ and} \tag{14}$$

$$a_g = \frac{p_g}{p^\ominus}, \forall g \in \Omega_G, \tag{15}$$

depending on the state of the modelled species. The reference concentration for both active materials is set to their respective maximal concentration of lithium in their solid phase $C^\ominus = C_{\text{max}}$. In all other cases the reference pressure and reference concentration is the standard thermodynamic reference state defined by the IUPAC as $p^\ominus = 100\,000\,\text{Pa}$ and $C^\ominus = 1000\,\text{mol}\,\text{m}^{-3}$, respectively [83]. Non-idealities, usually expressed by the activity or fugacity coefficient, may be present for the species; however, they are mostly not known yet and we thus neglect them in the here presented first study.

For the calculation of partial pressure, the mole fraction of each species within the gas phase is calculated as:

$$x_g'' = \frac{n_g''}{\sum_{\gamma \in \Omega_G} n_\gamma''}, \forall g \in \Omega_G. \tag{16}$$

The phase transition of the electrolytes' solvent components EC and EMC, and thus the molar amount of each solvent in both phases, is calculated using a phase equilibrium model of the binary mixture. A detailed explanation is given in the SI. For all other gaseous species such as CO_2 or C_2H_4, the solubility is modelled via Henry's law. Here, the solubility in both solvents is considered separately. The Henry coefficient $H_{g,\sigma}$ is hence used to obtain the mole fraction $x_{g,\sigma}'$ of the gaseous species g within the solvent σ as follows [84]:

$$x_{g,\sigma}' = \frac{p_g}{H_{g,\sigma}}, \forall g \in \Omega_G \backslash \Omega_{\text{Solv}} \wedge \forall \sigma \in \Omega_{\text{Solv}}. \tag{17}$$

Following, by rearranging Eqs. (16), (17) the total maximal amount $n_g'^{,\text{max}}$ of a gaseous species g in both solvents can be calculated as:

$$n_g'^{,\text{max}} = \sum_{\sigma \in \Omega_{\text{Solv}}} \frac{\frac{n_\sigma' \cdot p \cdot n_g}{H_{g,\sigma} \cdot \sum_{\gamma \in \Omega_G} n_\gamma}}{1 - \frac{(n_\sigma' \cdot p \cdot n_g)}{H_{g,\sigma} \cdot \sum_{\gamma \in \Omega_G} n_\gamma}}, \forall g \in \Omega_G \backslash \Omega_{\text{Solv}} \tag{18}$$

Since the gases are produced due to degradation reactions and are not present within the system from the start, we assume that they will stay dissolved until their respective solubility limit, expressed by the Henry coefficient, is reached. Thus, the calculation of the molar amount of each species in liquid and gas phase needs to be divided into two cases as shown below:

$$n_g', n_g'' = \begin{cases} n_g' = n_g, n_g'' = 0 & \text{for } n_g \leq n_g'^{,\text{max}} \\ n_g' = n_g'^{,\text{max}}, n_g'' = n_g - n_g'^{,\text{max}} & \text{for } n_g > n_g'^{,\text{max}} \end{cases}, \forall g \in \Omega_G \backslash \Omega_{\text{Solv}} \tag{19}$$

2.3.6. Changes in cell volume and pressure

In general, no pressure increase is assumed in the model due to use of an inflatable pouch cell. However, as there is a limit in the maximal pouch volume, above this value a pressure increase is expected. To monitor if and where this threshold is reached, the total gas volume is analysed. For this and the further analysis regarding the pressure rise due to evolving reaction gases, two phases need to be considered. First the isobaric time period in which the pouch cell volume increases due to the decomposition gases. And second the isochoric phase in which

Table 2
All species listed with their possible states, their respective initial amount and definition of the reference volume.

Species	States	$n_i(t=0)$ in mmol	Reference volume
$(CH_2OCO_2Li)_2$ (LEDC)	solid	0.723[b]	$V_{\text{SEI}} + V_{\text{AM,An.}}$
Li_2CO_3	solid	1.178[b]	$V_{\text{SEI}} + V_{\text{AM,An.}}$
LiF	solid	3.356[b]	$V_{\text{SEI}} + V_{\text{AM,An.}}$
$LiPF_6$	liquid	2.655[c]	$V_{\text{El.}}$
LiC_6	solid	24.605[c]	$V_{\text{AM,An.}}$
Li_zCoO_2	solid	21.670[c]	$V_{\text{AM,Cat.}}$
Co_3O_4	solid	0[a]	$V_{\text{AM,Cat.}}$
C_2H_4	liquid, gas	0[a]	$V_{\text{El.}}$
CO_2	liquid, gas	0[a]	$V_{\text{El.}}$
O_2	liquid, gas	0[a]	$V_{\text{El.}}$
H_2O	liquid, gas	0.0061[b]	$V_{\text{El.}}$
HF	liquid, gas	0[a]	$V_{\text{El.}}$
PF_5	liquid, gas	0[a]	$V_{\text{El.}}$
POF_3	liquid, gas	0[a]	$V_{\text{El.}}$
$C_3H_4O_3$ (EC)	liquid, gas	16.581[d]	$V_{\text{El.}}$
$C_4H_8O_3$ (EMC)	liquid, gas	10.095[d]	$V_{\text{El.}}$

[a] Assumed.
[b] Calculated based on assumptions given in text below.
[c] Calculated from structural data given in the SI.
[d] Calculated based on assumption of 1/1 v/v EC/EMC mixture.

the pouch cell reached its maximum volume and the gases contribute to a pressure rise. For this, the cell volume is calculated as

$$V_{\text{Cell}} = \begin{cases} V_{\text{Cell},0} + \sum_{g \in \Omega_G \backslash \Omega_{\text{Solv}}} \frac{n_g'' \cdot M_g}{\rho_g} & \text{for } V_{\text{Cell}} < V_{\text{Cell},0} \cdot 10 \\ V_{\text{Cell},0} \cdot 10 & \text{for } V_{\text{Cell}} \geq V_{\text{Cell},0} \cdot 10 \end{cases}. \tag{20}$$

Where $V_{\text{Cell},0}$ is the volume of the cell at the beginning of the experiment/simulation, ρ_g refers to the density of gaseous species g which is either calculated with Helmholtz models implemented in the CoolProp library or a version of the Peng–Robinson equation of state, see SI for more Information. The maximum cell volume is assumed to be 10 times the initial cell volume. This approximation is based on the measurement of Lee et al. who reported a sixfold increase of the pouch cell volume for cathode only NMC pouch cells stored at 90 °C for 4 h [85]. To prevent a too conservative assumption leading to a mistakenly high pressure increase and thus resulting high shift in the boiling temperature of the mixture, the tenfold increase in volume is chosen. Thus the calculation of the pressure follows to:

$$p = \begin{cases} 101\,325\,\text{Pa} = \text{const.} & \text{for } V_{\text{Cell}} < V_{\text{cell},0} \cdot 10 \\ 101\,325\,\text{Pa} + \frac{\sum_{g \in \Omega_G \backslash \{EC, EMC\}} n_g \cdot R \cdot T}{10 \cdot V_{\text{Cell},0}} & \text{for } V_{\text{Cell}} \geq V_{\text{cell},0} \cdot 10 \end{cases}. \tag{21}$$

The gas volume of the vaporized electrolytes' solvent compounds is not considered. This is done to isolate the influence of emerging degradation gases on the pressure and thus the possibility of vaporization. This calculations are, in combination with the binary phase equilibrium of EC and EMC, used to analyse if due to the pressure rise by evolving reaction gases, a phase transition would occur in such a system. Note that these considerations are not implemented in the model and are only analytical calculations performed on the gained results.

2.3.7. Initial conditions and implementation

Table 2 lists all initial values of all modelled species and their respective reference volumes used for calculating the concentrations. Underlying assumptions are marked with letters and added as footnotes. The initial temperature is given with $T_{t=0} = 40\,°\text{C}$ and the pressure is hold constant at $p = 101\,325\,\text{Pa}$.

The initial composition of the SEI is defined based on the knowledge that a pristine SEI mostly consists of organic species like LEDC and will

change its composition during aging to a more inorganic one. However, it is also known that a layer of LiF builds up very close to the surface of the anode. Thus it also takes up a certain volume of the pristine SEI. From this the following composition of the SEI given in volume fraction is assumed for the simulation, $\epsilon_{(CH_2OCO_2Li)_2} = 55\%$, $\epsilon_{Li_2CO_3} = 25\%$ and $\epsilon_{LiF} = 20\%$. Furthermore, the SEI thickness is assumed to be 50 nm which is the range of measured SEI thicknesses formed without VC as an additive [37,86,87].

No data on the actual amount of water in whole battery cells, neither for freshly assembled nor for aged ones, could be found in literature. It is known that electrolyte solutions contain a small amount of usually nowadays 20 ppm water. For our simulations, this value is further increased because of possible diffusion of water through the casing and the hygroscopic properties of the cathode material. 50 ppm H_2O are chosen under the assumption of a slightly aged cell [88,89].

Based on the assumptions listed in this section and the considerations regarding the general progression of all reactions discussed in Section 2.2 the kinetic parameters, k_0 and E_A, have been adjusted such that two constraints are met: The first one is that the reactions take place within the reported temperature interval for each given reaction. The second constraint is that the simulation, can reproduce the experimental data taken from Maleki et al. [17] as best as possible. Note that data points after the cell opening, marked as grey stars in Fig. 2, are excluded from the parameterization since the model, for now, cannot reproduce this phenomenon. Due to the difference in reported start temperatures for all reactions, a step-wise parameterization had to be performed. This has for reasons of complexity been performed by hand. Since two cases have been considered, one which assumed a battery case design which is highly inflatable (isobaric) and one that limits the inflation at 10 times the initial volume (isochoric), the parameterization has been performed twice. The kinetic parameters derived by parameterizing both cases against the available data can be found in the SI.

All presented model equations and parameters as well as presented submodels are implemented in MATLAB and the simulation was performed using the ode15s solver for stiff systems. All calculations have been performed with MATLAB Version 2020b [90], i7-9750H processor, 16 GB RAM. The average simulation time was between one to fifteen minutes.

3. Results and discussion

The upcoming section first compares temperature abuse simulations with experiments and analyses the predicted progression of reactions, their interplay and their contribution to temperature evolution during the abuse test. Here special focus is given to the transition from the HWS to exotherm mode. Thereafter, the pressure evolution and its impact on solvent boiling is analysed.

3.1. Process interplay and temperature evolution during thermal abuse

In Fig. 2, the experimental and simulated change of temperature during the ARC test are shown. The green crosses and grey stars illustrate the experimental data points before and after the cell opening, respectively.

Analysis starts at $T_0 = 40\,°C$, directly followed by a 10 °C heating step which in turn is followed by a 15 min wait period, and a 35 min seek period. This HWS pattern proceeds in the experiments until at 108 °C, marked by (I) in Fig. 2, an exothermic event leads to exothermic mode where the ARC follows the battery cell temperature. Due to insufficient heat production, the HWS modus starts again and at 110 °C an additional heating step is performed. Thereafter, other exothermic events lead to a steady but slow temperature increase from 119 °C until the experimental cell opening marked by a change in markers from green crosses to greys stars at 148 °C over the course of 12 h.
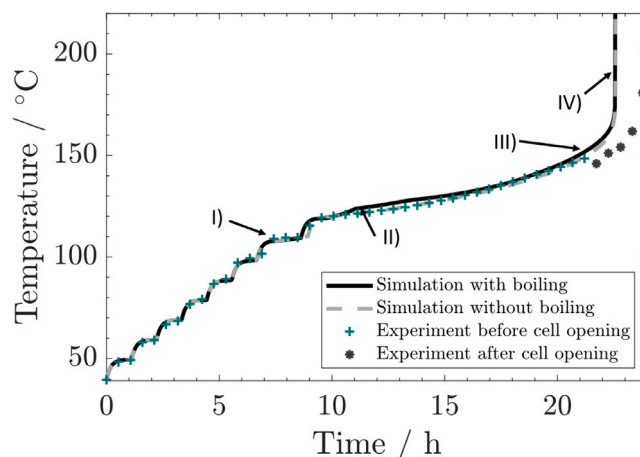

Fig. 2. Accelerated Rate Calorimetry measurement taken from Maleki et al. [17] and the parameterized model with (solid black line) and without (dashed grey line) boiling of electrolyte. Here, (I) marks the first transition from HWS to exotherm mode, (II) the deviation between simulation and experiment, (III) accelerated temperature increase (IV) the thermal runaway, respectively. (For interpretation of the references to colour in this figure legend, the reader is referred to the web version of this article.)

Cell opening leads to venting of the electrolyte and thus cooling of the battery [46,67,91]. This is assumed to take place here also, even though the temperature decrease and its correlation to cell opening was not discussed in the original publication. At this point the experiment shows a decrease of the temperature to 145 °C. This is followed by a further temperature increase leading to thermal runaway around 177 °C, marked with a (IV).

The isobaric simulation, i.e. represented by the solid black line, is in very good agreement with the experiments until around 119 °C, marked by a (II). Here, the simulation has a higher temperature gradient, and thus temperature, than the experiment. In the following, the gradient of the simulation is decreasing while the gradient of the experiment is increasing again. Therefore, the simulative curve is again in very good agreement with the experiment until the drop caused by cell opening. Since the here presented model is isobaric and can, thus, not reproduce cell opening, temperature deviation between experiment and simulation after cell opening is expected.

Evolution of the heat sources and sinks from individual processes that lead to the observed temperature progression. Here, especially the transition from HWS to exotherm mode, gives crucial insight into why cells run into thermal runaway and how this can be prevented. In Fig. 3(a), the endothermic (blue colours) and exothermic heats (red colours) and their sums are shown in respect to temperature, and the self-heating threshold that needs to be surpassed such that the ARC switches to exothermic mode. For better illustration, reactions and solvent boiling have been clustered, respectively. Individual contributions are given in the SI. The temperature horizon represents the temperature span in which the transition to the exothermic region occurs. Non-monotonous progression of heat evolution with local maxima and minima are observable throughout the simulation. These can be attributed to the unsteady heating: The heating steps increase the temperature of the system and, thus, the reaction rate of all reactions. In the following Wait and Seek period, the occurring reactions consume the reactants, leading to a reduction in reaction rates and with it the produced heats. The corresponding reactants for each reaction are shown in Fig. 3(b).

The first endothermic reaction taking place is the salt decomposition of $LiPF_6$ to PF_5 and LiF. The reaction rate exhibited in our simulation at 70 °C is comparable to one reported in experiments by
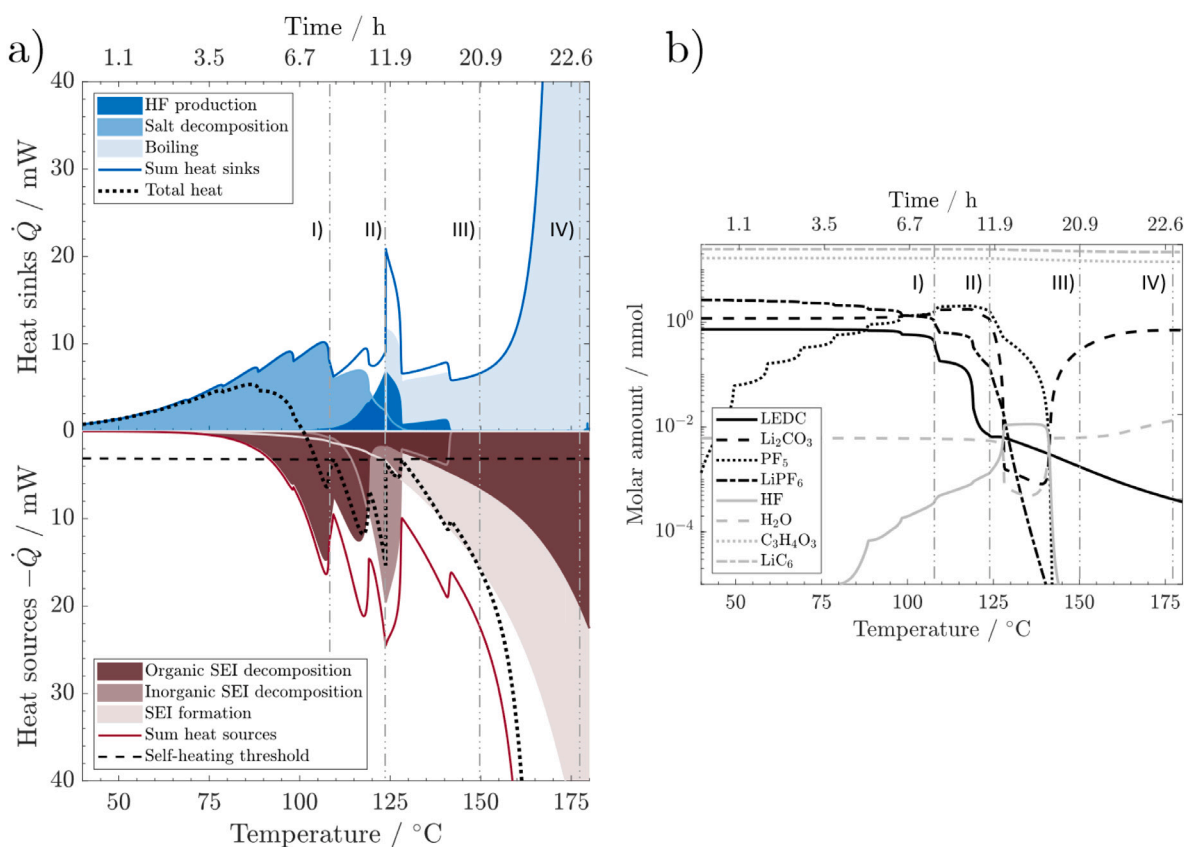
Fig. 3. (a) Isobaric simulation: produced endothermic and exothermic heats during the experiment leading to thermal runaway. Endothermic heats are presented in different shades of blue. Exothermic heats are shown in different shades of red. The sum of heat sinks and heat sources is shown in a solid line of blue and red, respectively. The sum of both together is represented by the dotted line. The self-heating threshold of the ARC is visualized by the dashed line. Inorganic and organic SEI formation as well as boiling of both solvents are lumped to SEI formation and boiling, respectively. (b) Evolution of molar amount of all reactants taking part in reactions illustrated in (a). (For interpretation of the references to colour in this figure legend, the reader is referred to the web version of this article.)

Sloop et al. [62]. However, in our simulation this reaction is, to a small extent, already present at around 40 °C. Thus, our results differ slightly from the reported temperature interval for the on-set of this reaction between 60 °C–80 °C. Considering additional side reactions, for example of the produced PF_5 with linear solvent components, could help reduce this observed difference between experiments and simulation. The first exothermic reaction is the organic SEI decomposition, where LEDC decomposes to Li_2CO_3 and gases at temperatures above 80 °C. In the beginning, the heat consumption due to salt decomposition prevails and the sum of heat sinks and sources, is endothermic. At around 105 °C, LEDC decomposition increases drastically, leading to an exothermic sum of heats. LEDC decomposition is thus identified as the reason for the first change from HWS to exothermic mode that was observed in experiments and simulation, confirming the theory of Richard et al. [56]. The subsequent steep decline in produced heat is due to slowed LEDC decomposition due to depletion of LEDC within the system as represented as a solid black line in Fig. 3(b) at (I). This causes, the sum of heats to approach the self-heating threshold around 110 °C, triggering a further heating step that can be observed in the experiment and simulation.

In the temperature region after the heating step around 120 °C, PF_5 and H_2O react to POF_3 and HF, and HF triggers inorganic SEI decomposition with Li_2CO_3 and HF reacting to LiF and H_2O. These reactions form an auto-catalytic cycle where HF production is endothermic and Li_2CO_3 decomposition is exothermic. The sum of both, however, is exothermic. This leads, in combination with fast kinetics in both reactions, to a peak in the sum of heats, causing the observable

deviation of isobaric simulation (i.e. with boiling) and experiment at (II) in Fig. 2 (see also discussion in next section). At 123 °C, the endothermic boiling of EC and EMC sets in. The immediate jump in endothermic heat leads to a drop of released heats without passing the self-heating threshold, therefore, no further heating step is performed. The exothermic formation of inorganic and organic SEI that sets in due to the primary decomposition of SEI, leads in the following to an increase in the sum of exothermic heats. Li_2CO_3 decomposition and HF production then both exhibit first a rapid decline and a slow rise in produced heat until at 142 °C both heats vanish. The underlying complex processes can be explained as follows. The reason for the sharp decline in inorganic SEI decomposition and HF production at 128 °C is that the concentration of Li_2CO_3 almost reached to zero, see the dashed black line in Fig. 3(b) at (II). Note that HF production depends on water production, which in turn is produced from Li_2CO_3. Further, both are limited by the production of Li_2CO_3. Until at 142 °C the amount of PF_5, represented as a dotted black line in Fig. 3(b), in the system is used up and the auto-catalytic cycle stops. This leads to the observable small dip in the sum of exothermic and endothermic heats. From then on the steady formation of both, the inorganic as well as organic SEI, and the subsequent re-decomposition of the organic SEI leads to a continuous increase in produced exothermic heat. This is partly counterweighted by the boiling solvent. However, the sum of both heats also increases steadily leading to the temperature increase that can be observed in the measurement.

Kupper et al. [35] already revealed that a set of two reactions, primary formation and decomposition of the SEI, does not release

sufficient heat to sustain the thermal runaway. They suggested that further side-reactions needed to be considered in order to simulate an ARC measurement. With the addition of conductive salt decomposition and subsequent side reactions such as the HF production and inorganic SEI decomposition we achieved this goal for the first time.

The solvent decomposition and cathode decomposition are not shown in Fig. 3 for reasons of better illustration. However, they are, also in this study, responsible for the thermal runaway occurring around 177 °C as already reported in literature [11,12,17] (see SI for individual reaction rates over the whole simulated temperature). Therefore, the general behaviour of all considered reactions, introduced and discussed in Section 2.2, could successfully be reproduced. This makes this model the first ever that is able to reproduce an ARC measurement solely based on chemical reactions, its participating species and their physical and chemical properties such as the heat of formation or heat capacity. Enabling us to in-depth analyse the interaction among them and draw the following conclusions.

The above description of occurring effects allows to reveal two competing phenomena. On the one hand, the rising temperature accelerates the dominating exothermic reactions, on the other hand, the acceleration of their underlying reactions leads to a decline in reactants concentration. Thus, we revealed how the concentration of main reactants, such as LEDC, can drastically influence the progression of thermal runaway in real accidents. This adds to the list of effects, such as gas venting and localization of internal short circuits, that make the thermal runaway and its propagation such an unpredictable phenomenon [69,92].

Additionally, the processes occurring in the analysed region can be classified into two groups, one which may be limited by reactant availability, and the other where sufficient reactant is available. The first group contains the organic and inorganic SEI decomposition as well as the conductive salt decomposition and the HF production. This first group includes all reactions that have a relatively low amount of reactants within the system and can therefore deplete early, leading to the fluctuating behaviour of the temperature gradient. Additionally, the reactants of these reactions can vary among different systems as well as between different cells of the same chemistry. For example LEDC, as the main SEI component, or H_2O as a contaminant can vary from cell to cell depending on different production environments and procedures or age of the cell. They make the thermal runaway particularly unpredictable. The second group contains the organic and inorganic formation of the SEI. Here, the reservoir of reactants is up to two orders of magnitudes higher, see Fig. 3(b), which means that these will not be used up during the early stages of thermal abuse, and will in turn lead to a monotonously increasing temperature gradient. Therefore, once these reactions are the main contributors to released heat, at temperatures 130 °C, and above, only rapid cooling can prevent the thermal runaway of the battery. The reactants, LiC_6 and EC, are among the components that differ the least among conventional Li-ion chemistries. Thus they do not, percentage-wise, vary as significantly between systems or even from cell to cell as the reactants of the first group. Thus, these reactions will, if activated by high temperatures, occur to more or less the same extent in all systems.

Eventually, the boiling of the electrolyte taking place at 123 °C uses up such a significant amount of heat that the gradient of the temperature changes noticeably. Thus, the occurring reactions are slowed down and the thermal runaway is delayed. On the other hand the reactions and their released gases might in return also influence the solvent boiling. This aspect is analysed in more detail in the upcoming section.

3.2. Pressure build-up and solvent boiling

While the model for now has been isobaric, due to the assumption of an infinitely inflatable pouch cell, evolving reaction gases in the real cell may have influenced the pressure and, thus, the boiling point

of the solvent mixture EC/EMC and the resulting contribution on the heat balance. In order to shed light on the impact of pressure, we here analyse in-depth a possible pressure increase and its impact on phase equilibrium and evaporative cooling during the heat abuse test.

Fig. 4(a) shows the progression of the relative volume increase and pressure during the temperature abuse test. Following our assumptions of a 10 times inflatable pouch cell, the evolving gases will first lead to a volume increase of the pouch-cell up to a maximum of 10 times its initial volume (region I). From then on, the system is assumed to be isochoric and the following evolving gases lead to an increase of the system pressure (region II). It can be observed that until 1.25 h, neither the volume ratio nor the pressure is increasing since no significant amount of gases are produced. Then, the volume increases continuously until it reaches the threshold of 10 times inflation at 7.3 h. The main contributing reactions are the decomposition of $LiPF_6$ and LEDC, since as discussed above, they are mainly occurring at this time. Following, the system pressure starts to rise with a steep gradient until 13.2 h. This is the timespan where most gas producing reactions are happening simultaneously, namely the conductive salt decomposition, HF production and the organic as well as inorganic SEI decomposition and production. The depletion of PF_5 and the subsequent decline of gas producing reaction such as HF production and the inorganic SEI decomposition leads to a more flat gradient until shortly before the end at 23 h, an almost vertical increase in pressure can be observed. This is correlated to the release of O_2 due to cathode decomposition, and the subsequent decomposition of the solvent species EC and EMC to CO_2 and H_2O.

The pressure evolution is taken as input for the binary phase equilibrium model to calculate the boiling point of the solvent. The evolution of the battery temperature relative to the boiling point of the solvent is shown in Fig. 4(b). The solvent composition of EC/EMC 50/50 (v/v), which was assumed in the experiment and used in simulation, is indicated by a black line. The threshold in relative temperature above which boiling occurs, i.e. $\frac{T}{T_b} > 1$ is visualized with a dashed line.

The step-wise temperature rise caused by the HWS mode of the ARC increases the relative temperature significantly from 0.3 to its first maximum of 0.85 at 7.3 h. This first maximum corresponds to the moment at which the maximum volume of the pouch cell is reached. Subsequently, the curve first declines to 0.8 due to the pressure increase, followed by a further small increase up to 0.82 at 9 h. Which is caused by the last heating step that occurs after the first minor exothermic event, see Fig. 2(I). The pressure increase then leads to a continuous decline to 0.75 at 17 h. At around 13 h, the point where due to depletion of PF_5, HF production as well as the inorganic SEI decomposition fade, the direction of the slope changes. Reactions such as HF production here take a special role: they are endothermic and thus slow down the temperature rise while at the same time they produce a significant amount of gases that contribute to the suppression of solvent boiling by a pressure increase. Thus, due to their decline and in general the reduction of simultaneously occurring reactions, the temperature rise starts to dominate over the increase in boiling point. Hereafter, the relative temperature increases sharply, corresponding to the thermal runaway, where the boiling point of the binary mixture is reached.

From this analysis it can be concluded that the investigated solvent mixture would not reach its boiling point before the thermal runaway. Thus, assuming a maximum inflatability of 10 times the initial pouch cell volume, phase transition does not take place and therefore does not influence the processes occurring during the HWS and self-heating phase of the thermal abuse test.

Solvent boiling is unlikely to occur before the final thermal runaway if the pouch cell is allowed to inflate. The absence of boiling in the experimental system could explain the deviations to the simulated
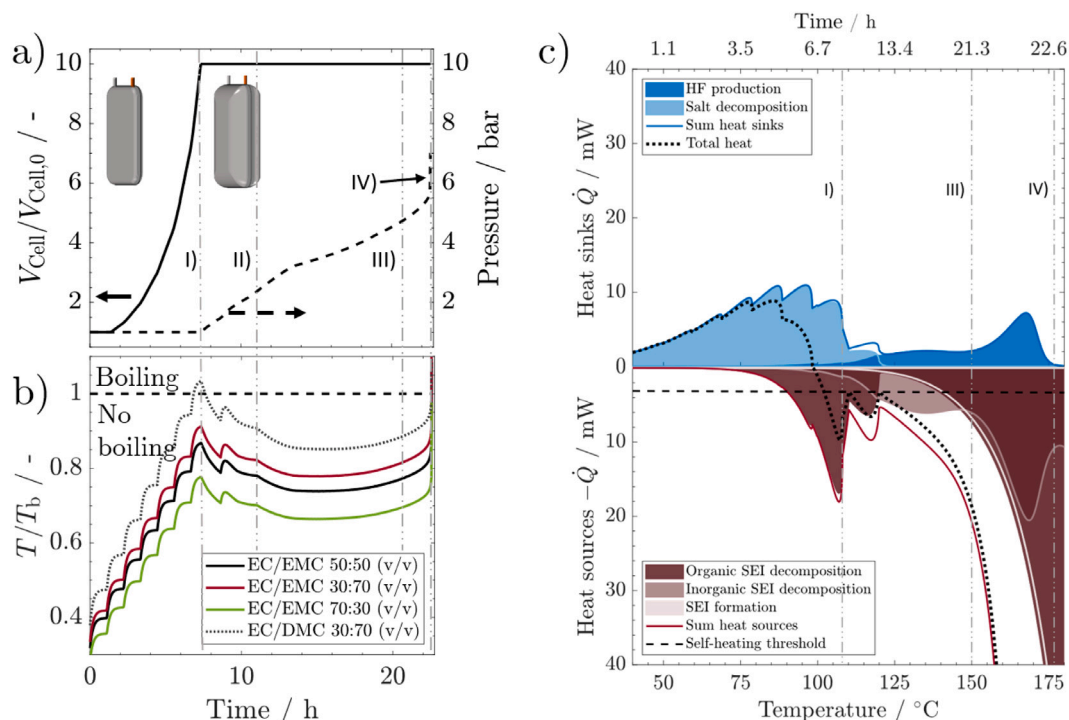
Fig. 4. (a) Evolution of the cell volume vs. its initial volume (solid line), and cell pressure with EC/EMC 30/70 (v/v) (b) Corresponding evolution of temperature relative to boiling temperature for various solvent compositions (c) Heat evolution over temperature for the re-parameterized case without solvent boiling with EC/EMC 30/70 (v/v). (For interpretation of the references to colour in this figure legend, the reader is referred to the web version of this article.)

temperature evolution in Fig. 2. The simulation shows a clear change in gradient of the temperature evolution caused by the onset of boiling. To evaluate, how the reactant and reaction evolution would be in the case without boiling and if a simulation without boiling can reproduce the experimental temperature evolution better, the presented model has been re-parameterized to the experimental data without solvent boiling. All kinetic parameters of both scenarios can be found in the SI. The results can be seen in Fig. 2 represented by the grey dashed line. In contrast to the model with boiling, the model without boiling now almost perfectly reproduces the experimental data points. In comparison to the scenario with boiling, the reaction kinetics of HF production, inorganic SEI decomposition and SEI formation are significantly slower, see Fig. 4. Here, the inorganic SEI decomposition and HF production even reach up to temperatures around 180 °C and higher. This results from the missing endothermic heat of solvent boiling which in the first scenario outweighed the faster kinetics. Note that, even though it seems that more heat is released by those two reactions without solvent boiling, this is not the case. The time it takes to change from 120 °C to 140 °C is around 8.7 h but to reach from 140 °C to 180 °C only 3.7 h.

Other solvent ratios of EC/EMC are also commonly used for batteries [93], the boiling point evolution has also been performed for EC/EMC 30/70 (v/v) and EC/EMC 70/30 (v/v) to check whether boiling would be expected for these compositions. As EC is still in excess in those cases, not much changes of the gas evolution was assumed and the same gas evolution was used for the calculations. Due to the fact that EMC is the lower boiling component of the mixture, the system with EC/EMC 30/70 (v/v) experiences an upwards shift and the EC/EMC 70/30 (v/v) shows a lower relative temperature. For both solvent compositions, the boiling point is also not reached before the thermal runaway. Therefore, it can further be concluded that it is highly unlikely that a mixture of these two solvents would start to boil

before the rapid thermal runaway sets in, if pressure is allowed to build up.

Besides the investigated solvent mixture, other types of linear carbonates such as dimethyl carbonate (DMC) are frequently used as co-solvents [93] instead of EMC. DMC has a lower boiling point than EMC. To evaluate whether boiling is expected for such systems, the same calculation has been performed with a binary equilibrium model of EC/DMC 30/70 (v/v). The result is shown in Fig. 4(b) as a dotted line. It can be observed that due to the lower boiling point of DMC, the boiling point of EC/DMC 30/70 (v/v) is reached before the maximum cell volume and thus before the pressure starts to rise. What this would mean for the further progression of the temperature evolution is a complex matter. Boiling would, due to its endothermic nature, on the one hand have a cooling effect which would delay thermal runaway. On the other hand, the comparably high amounts of gases released from solvent boiling would increase the pressure to an extent that would most probably suppress further boiling. All of the above shows that the electrolyte system used in this study, EC/EMC, is very unlikely to reach the boiling point before the thermal runaway.

Concluding, a pressure build-up during thermal abuse may prevent phase transition. As the cooling effect of boiling is missing, this may accelerate transition to thermal runaway. Whether boiling occurs depends strongly on battery composition, especially the solvent but also of certain reactants such as LEDC. Quantitative prediction will require further research such as to assess the impact of salts on the boiling point.

4. Conclusions

This study revealed the impact and interplay of exothermic reactions and solvent boiling during the thermal abuse of Li-ion batteries. We presented the first successful model approach to reproduce an ARC measurement rigorously based on the chemical components of a battery

and their thermodynamic properties. Here, especially in the early stages of self-heating, a fragile equilibrium between simultaneously occurring endothermic reactions, exothermic reactions and phenomena, such as solvent boiling, could be identified.

Occurring reactions could further be divided in two groups. Those, whose reactants are only present in small amounts. Prominent members of this group are reactions involving the SEI component LEDC and the contaminant H_2O. Due to the variance in their initial quantity, for example caused by fluctuations during production and formation, these reactants are among the causes that make the thermal runaway the unpredictable phenomenon it is. The other group contains the formation of SEI after its primary decay and its repeated decomposition. From the comparably high amount of the involved reactants, it follows that, once these reactions are activated by higher temperatures, only active cooling will prevent thermal runaway. Further, we shed light upon the probability of a possible phase transition and its impact on the temperature evolution during the self-heating phase. For the isobaric case, phase transition is shown to influence the course of the thermal runaway of an Li-ion battery, as its endothermic nature slows down self heating.

Gases released by degradation reactions may lead to rising pressure in the system and thus influence the phase transition behaviour. Assuming a 10 times inflatable pouch cell, the rising pressure completely suppressed solvent boiling until the final rapid thermal runaway phase for all EC/EMC solvent compositions of 30/70 to 70/30 volume ratio. However, for a lower boiling EC/DMC 30/70 (v/v) mixture, boiling of the electrolyte could be shown to occur already shortly before surpassing the self-heating threshold of the ARC. Therefore, we suggest to evaluate the behaviour of each electrolyte system individually. It could be shown that the complex interaction between gassing reactions, phase transition and eventually their impact on battery safety is an intricate phenomenon. The studies were conducted for cells without SEI forming additives such as VC. However, as mostly <1–2 wt.-% is used, they might be expected to have only a small impact on the thermal runaway behaviour. In conclusion the presented results should be transferable to chemistries including these additives. Not much research has so far been conducted on gas/liquid phase equilibria in batteries. However, this would be needed for a quantitative prediction of the electrolyte boiling and its impact on the thermal abuse behaviour. As a first measure to achieve this we propose to implement the pressure evolution explicitly into future models.

CRediT authorship contribution statement

F. Baakes: Conceptualization, Methodology, Software, Writing – original draft, Validation, Investigation, Visualization. **M. Lüthe:** Software, Validation, Data curation, Writing – original draft. **M. Gerasimov:** Methodology, Writing – review & editing. **V. Laue:** Supervision, Methodology. **F. Röder:** Conceptualization, Methodology, Visualization, Supervision. **P.B. Balbuena:** Methodology, Writing – review & editing. **U. Krewer:** Conceptualization, Writing – review & editing, Supervision, Funding acquisition.

Declaration of competing interest

The authors declare that they have no known competing financial interests or personal relationships that could have appeared to influence the work reported in this paper.

Acknowledgements

Appendix A. List of symbols

Symbols

Symbol	Description	Unit
a	Specific surface area/Activity	$m^2\,m^{-3}$/-
A	Area	m^2
α	Dissociation constant of $LiPF_6$	–
C_p	Heat capacity	$J\,K^{-1}$
c_p	Specific heat capacity	$J\,kg^{-1}\,K^{-1}$
$\underline{c}_p$	Molar heat capacity	$J\,mol^{-1}\,K^{-1}$
C	Concentration	$mol\,m^{-3}$
d	Thickness	m
E_A	Activation Energy	$kJ\,mol^{-1}$
ϵ	Volumetric fraction	–
$\Delta_f \underline{H}$	Enthalpy of formation	$kJ\,mol^{-1}$
$\Delta_r \underline{H}$	Enthalpy of reaction	$kJ\,mol^{-1}$
$\Delta_{vap}\underline{H}$	Enthalpy of vaporization	$kJ\,mol^{-1}$
H	Henry's coefficient	Pa
k	Pre-exponential frequency factor	$mol\,s^{-1}$
l	Length	m
m	Weight	kg
M	Molar weight	$mol\,kg^{-1}$
n	Moles	mol
ν	Stoichiometric factor	–
p	Pressure	Pa
q	Produced heat	W
r	Reaction rate/Radius	$mol\,s^{-1}$/m
R	Universal gas constant	$kJ\,mol^{-1}\,K^{-1}$
ρ	Density	$kg\,m^{-3}$
t	Time	s
T	Temperature	K
V	Volume	m^3
w	Width	m
x	Mole fraction	–
z	Lithium Intercalation fraction	–

Sets

Symbol	Description
Ω_{SP}	Set of all species
Ω_{RE}	Set of all reactions
Ω_G	Set of all gaseous species
Ω_L	Set of all liquid species
Ω_S	Set of all solid species
Ω_{Solv}	Set of all solvents
Ω_{SEI}	Set of all SEI species

Abbreviations

Symbol	Description
ARC	Accelerated Rate Calorimetry
DSC	Differential Scanning Calorimetry
EC	Ethylenecarbonate
EMC	Ethyl methyl carbonate
DMC	Dimethyl carbonate
HWS	Heat-Wait-Seek
LEDC	Lithium ethylene dicarbonate
SEI	Solid Electrolyte Interface
SI	Supporting Information

Appendix B. Supplementary data

Supplementary material related to this article can be found online at https://doi.org/10.1016/j.jpowsour.2021.230881.

References

[1] M. Winter, B. Barnett, K. Xu, Before Li ion batteries, Chem. Rev. 118 (23) (2018) 11433–11456.

[2] J.M. Tarascon, D. Guyomard, The $Li_{1+x}Mn_2O_4$/C rocking-chair system: a review, Electrochim. Acta 38 (9) (1993) 1221–1231.

[3] K. Brandt, Historical development of secondary lithium batteries, Solid State Ion. 69 (3–4) (1994) 173–183.

[4] J.M. Passerini, B. Scrosati, Plasticized carbon electrodes of interest for lithium rocking chair batteries, J. Power Sources 45 (3) (1993) 333–341.

[5] S.I. Tobishima, J.I. Yamaki, A consideration of lithium cell safety, J. Power Sources 81–82 (1999) 882–886.

[6] P. Biensan, B. Simon, J.P. Pérès, A. De Guibert, M. Broussely, J.M. Bodet, F. Perton, On safety of lithium-ion cells, J. Power Sources 81–82 (1999) 906–912.

[7] D.D. MacNeil, Comparison of the reactivity of various carbon electrode materials with electrolyte at elevated temperature, J. Electrochem. Soc. 146 (10) (1999) 3596.

[8] P.G. Balakrishnan, R. Ramesh, T. Prem Kumar, Safety mechanisms in lithium-ion batteries, J. Power Sources 155 (2) (2006) 401–414.

[9] A.W. Golubkov, D. Fuchs, J. Wagner, H. Wiltsche, C. Stangl, G. Fauler, G. Voitic, A. Thaler, V. Hacker, Thermal-runaway experiments on consumer batteries with metal-oxide and olivin-type cathodes, RSC Adv. 4 (7) (2014) 3633–3642.

[10] A.W. Golubkov, S. Scheikl, R. Planteu, G. Voitic, H. Wiltsche, C. Stangl, G. Fauler, A. Thaler, V. Hacker, Thermal runaway of commercial 18650 batteries with LFP and NCA cathodes - impact of state of charge and overcharge, RSC Adv. 5 (70) (2015) 57171–57186.

[11] D. Ren, X. Liu, X. Feng, L. Lu, M. Ouyang, J. Li, X. He, Model-based thermal runaway prediction of lithium-ion batteries from kinetics analysis of cell components, Appl. Energy 228 (2018) 633–644.

[12] A. Kriston, I. Adanouj, V. Ruiz, A. Pfrang, Quantification and simulation of thermal decomposition reactions of Li-ion battery materials by simultaneous thermal analysis coupled with gas analysis, J. Power Sources 435 (June) (2019) 226774.

[13] K. Tweed, Tesla's lithium-ion battery catches fire, Spectrum.Ieee.Org, spectrum.ieee.org, visited on 02.04.2020, 2013.

[14] A. Tutu, BMW i8 Catches Fire in The Netherlands, Firefighters Drop It in Water Container, Autorevolution.Com, autorevolution.com, visited on 02.04.2020, 2019.

[15] A. Reid, Porsche Taycan EV catches fire and burns down garage in Florida, Driving.Ca, driving.ca, visited on 02.04.2020, 2020.

[16] S. Solchenbach, M. Metzger, M. Egawa, H. Beyer, H.a. Gasteiger, Quantification of PF_5 and POF_3 from side reactions of $LiPF_6$ in Li-Ion batteries, J. Electrochem. Soc. 165 (13) (2018) A3022–A3028.

[17] H. Maleki, G. Deng, A. Anani, J. Howard, Thermal stability studies of Li-ion cells and components, J. Electrochem. Soc. 146 (9) (1999) 3224.

[18] T. Kawamura, S. Okada, J. Yamaki, Decomposition reaction of $LiPF_6$-based electrolytes for lithium ion cells, J. Power Sources 156 (2) (2006) 547–554.

[19] A. Veluchamy, C.H. Doh, D.H. Kim, J.H. Lee, H.M. Shin, B.S. Jin, H.S. Kim, S.I. Moon, Thermal analysis of Li_xCoO_2 cathode material of lithium ion battery, J. Power Sources 189 (1) (2009) 855–858.

[20] Y. Baba, S. Okada, J. Yamaki, Thermal stability of Li_xCoO_2 cathode for lithium ion battery, Solid State Ion. 148 (3–4) (2002) 311–316.

[21] H. Yang, G.V. Zhuang, P.N. Ross, Thermal stability of $LiPF_6$ salt and Li-ion battery electrolytes containing $LiPF_6$, J. Power Sources 161 (1) (2006) 573–579.

[22] J. Diekmann, S. Doose, S. Weber, S. Münch, W. Haselrieder, A. Kwade, Development of a new procedure for nail penetration of Lithium-Ion cells to obtain meaningful and reproducible results, J. Electrochem. Soc. 167 (9) (2020) 090504.

[23] I. Avdeev, M. Gilaki, Structural analysis and experimental characterization of cylindrical lithium-ion battery cells subject to lateral impact, J. Power Sources 271 (2014) 382–391.

[24] T.D. Hatchard, D.D. MacNeil, A. Basu, J.R. Dahn, Thermal model of cylindrical and prismatic lithium-ion cells, J. Electrochem. Soc. 148 (7) (2002) A755.

[25] M.N. Richard, J.R. Dahn, Accelerating rate calorimetry study on the thermal stability of lithium intercalated graphite in electrolyte. II. Modeling the results and predicting differential scanning calorimeter curves, J. Electrochem. Soc. 146 (6) (1999) 2078.

[26] D.D. MacNeil, J.R. Dann, J.R. Dahn, Test of reaction kinetics using both differential scanning and accelerating rate calorimetries as applied to the reaction of Li_xCoO_2 in non-aqueous electrolyte, J. Phys. Chem. A 105 (18) (2002) 4430–4439.

[27] R. Spotnitz, J. Franklin, Abuse behavior of high-power, lithium-ion cells, J. Power Sources 113 (1) (2003) 81–100.

[28] G.H. Kim, A. Pesaran, R. Spotnitz, A three-dimensional thermal abuse model for lithium-ion cells, J. Power Sources 170 (2) (2007) 476–489.

[29] A. Melcher, C. Ziebert, M. Rohde, H.J. Seifert, Modeling and simulation of the thermal runaway behavior of cylindrical Li-ion cells-computing of critical parameters, Energies 9 (4) (2016) 1–19.

[30] S. Abada, G. Marlair, A. Lecocq, M. Petit, V. Sauvant-Moynot, F. Huet, Safety focused modeling of lithium-ion batteries: A review, J. Power Sources 306 (2016) 178–192.

[31] X. Feng, L. Lu, M. Ouyang, J. Li, X. He, A 3D thermal runaway propagation model for a large format lithium ion battery module, Energy 115 (2016) 194–208.

[32] P.T. Coman, E.C. Darcy, C.T. Veje, R.E. White, Numerical analysis of heat propagation in a battery pack using a novel technology for triggering thermal runaway, Appl. Energy 203 (2017) 189–200.

[33] M. Zhang, L. Liu, A. Stefanopoulou, J. Siegel, L. Lu, X. He, M. Ouyang, Fusing phenomenon of lithium-ion battery internal short circuit, J. Electrochem. Soc. 164 (12) (2017) A2738–A2745.

[34] P.T. Coman, E.C. Darcy, C.T. Veje, R.E. White, Modelling Li-ion cell thermal runaway triggered by an internal short circuit device using an efficiency factor and arrhenius formulations, J. Electrochem. Soc. 164 (4) (2017) A587–A593.

[35] C. Kupper, S. Spitznagel, H. Döring, M.a. Danzer, C. Gutierrez, A. Kvasha, W.G. Bessler, Combined modeling and experimental study of the high-temperature behavior of a lithium-ion cell: Differential scanning calorimetry, accelerating rate calorimetry and external short circuit, Electrochim. Acta 306 (2019) 209–219.

[36] Y. Wang, S. Nakamura, M. Ue, P.B. Balbuena, Theoretical studies to understand surface chemistry on carbon anodes for lithium-ion batteries: reduction mechanisms of ethylene carbonate, J. Am. Chem. Soc. 123 (47) (2001) 11708–11718.

[37] F.A. Soto, Y. Ma, J.M. Martinez de la Hoz, J.M. Seminario, P.B Balbuena, Formation and growth mechanisms of solid-electrolyte interphase layers in rechargeable batteries, Chem. Mater. 27 (23) (2015) 7990–8000.

[38] F. Röder, R.D. Braatz, U. Krewer, Multi-scale simulation of heterogeneous surface film growth mechanisms in lithium-ion batteries, J. Electrochem. Soc. 164 (11) (2017) E3335.

[39] F. Röder, V. Laue, U. Krewer, Model based multiscale analysis of film formation in Lithium-ion batteries, Batter. Supercaps 2 (3) (2019) 248–265.

[40] J. Geppert, F. Kubannek, P. Röse, U. Krewer, Identifying the oxygen evolution mechanism by microkinetic modelling of cyclic voltammograms, Electrochim. Acta 380 (2021) 137902.

[41] P. Schön, U. Krewer, Revealing the complex sulfur reduction mechanism using cyclic voltammetry simulation, Electrochim. Acta 373 (2021) 137523.

[42] N. Tanaka, W.G. Bessler, Numerical investigation of kinetic mechanism for runaway thermo-electrochemistry in lithium-ion cells, Solid State Ion. (2013).

[43] W.G. Kupper, Multi-scale thermo-electrochemical modeling of performance and aging of a $LiFePO_4$/graphite lithium-ion cell, J. Electrochem. Soc. 164 (2) (2017) A304–A320.

[44] F. Röder, R.D. Braatz, U. Krewer, Direct coupling of continuum and kinetic Monte Carlo models for multiscale simulation of electrochemical systems, Comput. Chem. Eng. 121 (2019) 722–735.

[45] X. He, D. Bresser, S. Passerini, F. Baakes, U. Krewer, J. Lopez, C.T. Mallia, Y. Shao-Horn, I. Cekic-Laskovic, S. Wiemers-Meyer, F.A. Soto, V. Ponce, J.M. Seminario, P.B. Balbuena, H. Jia, W. Xu, Y. Xu, C. Wang, B. Horstmann, R. Amine, C. Su, J. Shi, K. Amine, M. Winter, A. Latz, R. Kostecki, The passivity of lithium electrodes in liquid electrolytes for secondary batteries, Nat. Rev. Mater. 6 (2021) 1036–1052.

[46] P.T. Coman, S. Rayman, R.E. White, A lumped model of venting during thermal runaway in a cylindrical lithium Cobalt Oxide lithium-ion cell, J. Power Sources 307 (2016) 56–62.

[47] P.T. Coman, S. Mátéfi-Tempfli, C.T. Veje, R.E. White, Modeling vaporization, gas generation and venting in Li-Ion battery cells with a dimethyl carbonate electrolyte, J. Electrochem. Soc. 164 (9) (2017) A1858–A1865.

[48] B. Lei, W. Zhao, C. Ziebert, N. Uhlmann, M. Rohde, H.J. Seifert, Experimental analysis of thermal runaway in 18650 cylindrical Li-Ion cells using an accelerating rate calorimeter, Batteries 3 (4) (2017) 14.

[49] O.S. Mendoza-Hernandez, H. Ishikawa, Y. Nishikawa, Y. Maruyama, M. Umeda, Cathode material comparison of thermal runaway behavior of Li-ion cells at different state of charges including over charge, J. Power Sources 280 (2015) 499–504.

[50] M. Fleischhammer, T. Waldmann, G. Bisle, B.I. Hogg, M. Wohlfahrt-Mehrens, Interaction of cyclic ageing at high-rate and low temperatures and safety in lithium-ion batteries, J. Power Sources 274 (2015) 432–439.

[51] M. Börner, A. Friesen, M. Grützke, Y.P. Stenzel, G. Brunklaus, J. Haetge, S. Nowak, F.M. Schappacher, M. Winter, Correlation of aging and thermal stability of commercial 18650-type lithium ion batteries, J. Power Sources 342 (2017) 382–392.

[52] D.I. Townsend, J.C. Tou, Thermal hazard evaluation by an accelerating rate calorimeter, Thermochim. Acta 37 (1) (1980) 1–30.

[53] B. Simon, I.L. Moulineaux, J. Boeuve, Rechargable lithium electrochemical cell, United States Patent 5, 626, 981, 1998.

[54] D. Aurbach, K. Gamolsky, B. Markovsky, Y. Gofer, M. Schmidt, U. Heider, On the use of vinylene carbonate (VC) as an additive to electrolyte solutions for Li-ion batteries, Electrochim. Acta 47 (9) (2002) 1423–1439.

[55] A.M. Andersson, K. Edström, Chemical composition and morphology of the elevated temperature SEI on graphite, J. Electrochem. Soc. 148 (10) (2001) 1100–1109.

[56] M.N. Richard, J.R. Dahn, Predicting electrical and thermal abuse behaviours of practical lithium-ion cells from accelerating rate calorimeter studies on small samples in electrolyte, Vol. 79, No. 2, 1999, pp. 135–142.

[57] K. Kanamura, S. Shiraishi, Z.I. Takehara, Electrochemical deposition of very smooth lithium using nonaqueous electrolytes containing HF, J. Electrochem. Soc. 143 (7) (1996) 2187–2197.

[58] Na. Choi, I.A. Profatilova, S. Kim, E. Song, Thermal reactions of lithiated graphite anode in LiPF$_6$-based electrolyte, Thermochim. Acta 480 (1–2) (2008) 10–14.

[59] D. Aurbach, A. Zaban, Y. Ein-Eli, I. Weissman, O. Chusid, B. Markovsky, M. Levi, E. Levi, A. Schechter, E. Granot, Recent studies on the correlation between surface chemistry, morphology, three-dimensional structures and performance of Li and Li-C intercalation anodes in several important electrolyte systems, J. Power Sources 68 (1) (1997) 91–98.

[60] D. Aurbach, B. Markovsky, A. Shechter, Y. Ein-Eli, H. Cohen, A comparative study of synthetic graphite and Li electrodes in electrolyte solutions based on ethylene carbonate-dimethyl carbonate mixtures, J. Electrochem. Soc. 143 (12) (1996) 3809.

[61] M. Stich, M. Göttlinger, M. Kurniawan, U. Schmidt, A. Bund, Hydrolysis of LiPF$_6$ in carbonate-based electrolytes for lithium-ion batteries and in aqueous media, J. Phys. Chem. C 122 (16) (2018) 8836–8842.

[62] S.E. Sloop, J.K. Pugh, S. Wang, J.B. Kerr, K. Kinoshita, Chemical reactivity of PF5 and LiPF$_6$ in ethylene carbonate/dimethyl carbonate solutions, Electrochem. Solid-State Lett. 4 (4) (2001) 62–64.

[63] K. Tasaki, K. Kanda, S. Nakamura, M. Ue, Decomposition of LiPF$_6$ and stability of PF$_5$ in Li-Ion battery electrolytes, J. Electrochem. Soc. 150 (12) (2003) A1628.

[64] Y. Okamoto, Ab initio calculations of thermal decomposition mechanism of LiPF$_6$-based electrolytes for lithium-ion batteries, J. Electrochem. Soc. 160 (2) (2013) 404–409.

[65] H. Arai, S. Okada, Y. Sakurai, J. Yamaki, Thermal behavior of Li$_{1-x}$NiO$_2$ and the decomposition mechanism, Solid State Ion. 109 (3–4) (1998) 295–302.

[66] D.G Kellerman, V.V. Karelina, V.S. Gorshkov, Y.N. Blinovskov, Investigation of thermal stability of LiCoO$_2$ and Li$_{1-x}$CoO$_2$, Chem. Sustain. Dev. 10 (2002) 721–726.

[67] D.P. Abraham, E.P. Roth, R. Kostecki, K. McCarthy, S. MacLaren, D.H. Doughty, Diagnostic examination of thermally abused high-power lithium-ion cells, J. Power Sources 161 (1) (2006) 648–657.

[68] W.C. Chen, Y.W. Wang, C.M. Shu, Adiabatic calorimetry test of the reaction kinetics and self-heating model for 18650 Li-ion cells in various states of charge, J. Power Sources 318 (2016) 200–209.

[69] X. Feng, M. Ouyang, X. Liu, L. Lu, Y. Xia, X. He, Thermal runaway mechanism of lithium ion battery for electric vehicles: A review, Energy Storage Mater. 10 (May 2017) (2018) 246–267.

[70] T. Yoon, M.S. Milien, B.S. Parimalam, B.L. Lucht, Thermal decomposition of the solid electrolyte interphase (SEI) on silicon electrodes for Lithium Ion batteries, Chem. Mater. 29 (7) (2017) 3237–3245.

[71] R. Jung, F. Linsenmann, R. Thomas, J. Wandt, S. Solchenbach, F. Maglia, C. Stinner, M. Tromp, H.A. Gasteiger, Nickel, manganese, and cobalt dissolution from Ni-rich NMC and their effects on NMC622-graphite cells, J. Electrochem. Soc. 166 (2) (2019) A378.

[72] G.G. Eshetu, S. Grugeon, G. Gachot, D. Mathiron, M. Armand, S. Laruelle, LiFSI vs. LiPF$_6$ electrolytes in contact with lithiated graphite: Comparing thermal stabilities and identification of specific SEI-reinforcing additives, Electrochim. Acta 102 (2013) 133–141.

[73] M.M. Kabir, D.E. Demirocak, Degradation mechanisms in Li-ion batteries: a state-of-the-art review, Int. J. Energy Res. 41 (14) (2017) 1963–1986.

[74] S. Wiemers-Meyer, S. Jeremias, M. Winter, S. Nowak, Influence of battery cell components and water on the thermal and chemical stability of LiPF$_6$ based lithium ion battery electrolytes, Electrochim. Acta 222 (2016) 1267–1271.

[75] G.H. Hess, Recherches thermochimiques, Bull. Sci. Acad. Impériale Sci. 8 (1840) 257–272.

[76] ICP622540PMT, in: Renata Batteries Datasheet, Vol. 41, 2019, 622540.

[77] A.M. Colclasure, R.J. Kee, Thermodynamically consistent modeling of elementary electrochemistry in lithium-ion batteries, Electrochim. Acta 55 (28) (2010) 8960–8973.

[78] B. Rieger, S. Schlueter, S.V. Erhard, J. Schmalz, G. Reinhart, A. Jossen, Multi-scale investigation of thickness changes in a commercial pouch type lithium-ion battery, J. Energy Storage 6 (2016) 213–221.

[79] H. Maleki, J.N. Howard, Role of the cathode and anode in heat generation of Li-ion cells as a function of state of charge, J. Power Sources 137 (1) (2004) 117–127.

[80] S. Arrhenius, Über die Dissociationswärme und den Einfluss der Temperatur auf den Dissociationsgrad der Elektrolyte, Z. Phys. Chem. 4U (1) (1889).

[81] H.S. Fogler, Elements of Chemical Reaction Engineering, third ed., Prentice Hall PTR, ©1999, Upper Saddle River, N.J., 2016.

[82] J. Dalton, Essay IV. On the expansion of elastic fluids by heat, Mem. Lit. Philos. Soc. Manch. 5 (2) (1802) 595–602.

[83] A.D. McNaught, A. Wilkinson, IUPAC. Compendium of Chemical Terminology, 2nd ed., Blackwell Scientific Publications, 1997, (the "Gold Book").

[84] W. Henry, Experiments on the quantity of gases absorbed by water at different tempratus, and under different pressur, Philos. Trans. R. Soc. Lond. 93 (1803) 29–42.

[85] K.H. Lee, E.H. Song, J.Y. Lee, B.H. Jung, H.S. Lim, Mechanism of gas build-up in a Li-ion cell at elevated temperature, J. Power Sources 132 (1–2) (2004) 201–205.

[86] D. Aurbach, Y. Ein-Eli, B. Markovsky, A. Zaban, S. Luski, Y. Carmeli, H. Yamin, The study of electrolyte solutions based on ethylene and diethyl carbonates for rechargeable Li batteries: II. Graphite electrodes, J. Electrochem. Soc. 142 (9) (1995) 2882.

[87] M. Nie, D. Chalasani, D.P. Abraham, Y. Chen, A. Bose, B.L. Lucht, Lithium ion battery graphite solid electrolyte interphase revealed by microscopy and spectroscopy, J. Phys. Chem. C 117 (3) (2013) 1257–1267.

[88] U. Heider, R. Oesten, M. Jungnitz, Challenge in manufacturing electrolyte solutions for lithium and lithium ion batteries quality control and minimizing contamination level, J. Power Sources 81–82 (1999) 119–122.

[89] D. Aurbach, I. Weissman, A. Zaban, P. Dan, On the role of water contamination in rechargeable Li batteries, Electrochim. Acta 45 (7) (1999) 1135–1140.

[90] MATLAB, Version 9.9.0.1570001 (R2020b), The MathWorks Inc. Natick, Massachusetts, 2020.

[91] X. Liu, S.I. Stoliarov, M. Denlinger, A. Masias, K. Snyder, Comprehensive calorimetry of the thermally-induced failure of a lithium ion battery, J. Power Sources 280 (2015) 516–525.

[92] S. Wilke, B. Schweitzer, S. Khateeb, S. Al-Hallaj, Preventing thermal runaway propagation in lithium ion battery packs using a phase change composite material: An experimental study, J. Power Sources 340 (2017) 51–59.

[93] J. Kalhoff, G.G. Eshetu, D. Bresser, S. Passerini, Safer electrolytes for lithium-ion batteries: state of the art and perspectives, ChemSusChem 8 (13) (2015) 2154–2175.